The zebrafish *grime* mutant uncovers an evolutionarily conserved role for Tmem161b in the control of cardiac rhythm

Charlotte D. Koopman[a,b,1], Jessica De Angelis[c,1], Swati P. Iyer[c,d,1], Arie O. Verkerk[e], Jason Da Silva[c], Geza Berecki[f,g], Angela Jeanes[c], Gregory J. Baillie[c], Scott Paterson[c], Veronica Uribe[d], Ophelia V. Ehrlich[d], Samuel D. Robinson[c], Laurence Garric[a], Steven Petrou[f,g], Cas Simons[c,h], Irina Vetter[c,i], Benjamin M. Hogan[c,j], Teun P. de Boer[b], Jeroen Bakkers[a,b], and Kelly A. Smith[c,d,2]

[a]Department of Cardiac Development and Genetics, Hubrecht Institute, University Medical Centre Utrecht, Utrecht 3584 CT, The Netherlands; [b]Department of Medical Physiology, Division of Heart & Lungs, University Medical Center, Utrecht 3584 CM, The Netherlands; [c]Institute for Molecular Bioscience, The University of Queensland, Brisbane, QLD 4072, Australia; [d]Department of Physiology, The University of Melbourne, Parkville, VIC 3010, Australia; [e]Department of Medical Biology, Amsterdam University Medical Centre, 1105 AZ Amsterdam, The Netherlands; [f]The Florey Institute of Neuroscience and Mental Health, The University of Melbourne, Parkville, VIC 3010, Australia; [g]Department of the Florey Institute, The University of Melbourne, Parkville, VIC 3010, Australia; [h]Genetics Theme, Murdoch Children's Research Institute, Parkville, VIC 3010, Australia; [i]School of Pharmacy, The University of Queensland, Brisbane, QLD 4102, Australia; and [j]Peter MacCallum Cancer Centre, The University of Melbourne, Parkville, VIC 3010, Australia

Edited by Lily Yeh Jan, University of California, San Francisco, CA, and approved December 30, 2020 (received for review August 31, 2020)

The establishment of cardiac function in the developing embryo is essential to ensure blood flow and, therefore, growth and survival of the animal. The molecular mechanisms controlling normal cardiac rhythm remain to be fully elucidated. From a forward genetic screen, we identified a unique mutant, *grime*, that displayed a specific cardiac arrhythmia phenotype. We show that loss-of-function mutations in *tmem161b* are responsible for the phenotype, identifying Tmem161b as a regulator of cardiac rhythm in zebrafish. To examine the evolutionary conservation of this function, we generated knockout mice for Tmem161b. Tmem161b knockout mice are neonatal lethal and cardiomyocytes exhibit arrhythmic calcium oscillations. Mechanistically, we find that Tmem161b is expressed at the cell membrane of excitable cells and live imaging shows it is required for action potential repolarization in the developing heart. Electrophysiology on isolated cardiomyocytes demonstrates that Tmem161b is essential to inhibit Ca^{2+} and K^+ currents in cardiomyocytes. Importantly, Tmem161b haploinsufficiency leads to cardiac rhythm phenotypes, implicating it as a candidate gene in heritable cardiac arrhythmia. Overall, these data describe Tmem161b as a highly conserved regulator of cardiac rhythm that functions to modulate ion channel activity in zebrafish and mice.

cardiac | arrhythmia | zebrafish | mouse | forward genetics

Model organism research has discovered a wealth of information about the molecular control of cardiac morphogenesis. Both forward and reverse genetics approaches have identified a vast number of genes that are essential for cardiac development (1–3). By contrast, far fewer genes have been identified for their role in cardiac function during development (4). This may be due, in part, to the relative ease of examining morphology, which facilitates high-throughput screening approaches, compared with the more time-consuming and complicated assays required to assess cardiac function, such as cardiac arrhythmias.

Recently, a number of advancements have improved phenotypic analysis and screening approaches, assisting in the examination of cardiac arrhythmia phenotypes. High-speed imaging has progressed significantly and, when combined with new optogenetic reporters, sophisticated cardiac electrophysiology is achievable in the live animal (5–7). Defined chemical libraries and CRISPR-Cas9 mutagenesis have extended this analysis to include pharmacological and molecular analyses (4, 8, 9). These approaches have been applied elegantly to model known genetic causes of cardiac arrhythmia and, importantly, to screen for inhibitors of the phenotypes in these models (10–12). Despite these advancements, however, there have been few discoveries of completely unexpected new genes from model organisms in cardiac rhythm over the past decade.

To keep the heart rhythmic, action potentials (APs) propagate across the heart in a carefully patterned manner. They begin in the sinoatrial node (SAN), a unique structure of the heart capable of initiating action potentials spontaneously and with clocklike rhythm (the "pacemaker"). From the SAN, action potentials travel to the atrial chambers and spread to atrial cardiomyocytes, triggering them to contract. Simultaneously, action potentials travel to the atrioventricular node (AVN), where they are delayed. This delay is essential: it permits time for the atria to contract and blood to fill the ventricles. Action potentials are then initiated in the AVN (which also has pacemaking ability) and spread to the

Significance

The heart initiates rhythmic contractions early during development. A unique zebrafish mutant with specific cardiac arrhythmia phenotypes was identified and mutation of the uncharacterized *tmem161b* gene shown to be causative. Tmem161b knockout mice are perinatal lethal and isolated embryonic cardiomyocytes exhibit arrhythmic Ca^{2+} oscillations, suggesting functional conservation. Protein localization studies show Tmem161b is expressed in excitable cells and at cardiomyocyte plasma membranes. Imaging of in vivo action potentials shows *tmem161b* mutants have prolonged action potential repolarization. Patch-clamping of isolated cardiomyocytes confirms prolonged action potential repolarization and shows increased Ca^{2+} and K^+ currents are likely the cause of altered action potential morphology. This suggests Tmem161b is a new conserved regulator of cardiac rhythm by inhibiting Ca^{2+} and K^+ currents.

Author contributions: C.D.K., J.D.A., S.P.I., A.O.V., J.D.S., G.B., A.J., G.J.B., S. Paterson, V.U., C.S., I.V., B.M.H., T.P.d.B., J.B., and K.A.S. designed research; C.D.K., J.D.A., S.P.I., A.O.V., J.D.S., G.B., G.J.B., S. Paterson, V.U., O.V.E., S.D.R., L.G., I.V., and K.A.S. performed research; J.D.A., S.P.I., J.D.S., G.B., A.J., G.J.B., S. Paterson, S. Petrou, C.S., B.M.H., T.P.d.B., J.B., and K.A.S. contributed new reagents/analytic tools; C.D.K., J.D.A., S.P.I., A.O.V., J.D.S., G.B., G.J.B., V.U., O.V.E., S.D.R., L.G., I.V., B.M.H., T.P.d.B., J.B., and K.A.S. analyzed data; and C.D.K., J.D.A., S.P.I., A.O.V., G.B., B.M.H., T.P.d.B., J.B., and K.A.S. wrote the paper.

The authors declare no competing interest.

This article is a PNAS Direct Submission.

[1]C.D.K., J.D.A., and S.P.I. contributed equally to this work.

[2]To whom correspondence may be addressed. Email: kelly.smith1@unimelb.edu.au.

This article contains supporting information online at https://www.pnas.org/lookup/suppl/doi:10.1073/pnas.2018220118/-/DCSupplemental.

Published February 17, 2021.

ventricular cardiomyocytes, signaling to sarcomeres to contract almost synchronously. While there are considerable differences between species at an anatomical level, at a coarse level this arrangement of action potential propagation (SAN > atrium > AVN > ventricle) is conserved (13). Perhaps more importantly, the genetics and electrophysiology of the action potential is also highly conserved (9, 14).

The similarities between zebrafish and human cardiac electrophysiology make the zebrafish an excellent model for gene discovery in this process. It boasts many advantages that make it excellent for high-throughput screening (7) and, importantly, zebrafish and humans have similar heart rate and action potential characteristics, making it perhaps superior to mice in this regard (14, 15). Using this rationale, we have performed a forward genetic screen to identify regulators of cardiac rhythm. Here, we describe the discovery of a regulator of cardiac rhythm: *transmembrane protein 161b* (*tmem161b*) and demonstrate that it functions in maintaining cardiac rhythm by inhibiting K^+ and Ca^{2+} currents.

Results

***grime* Mutants Display Highly Specific Cardiac Arrhythmia.** To identify genetic regulators of cardiac rhythm, we conducted a forward genetic screen in zebrafish. Embryos, 6 days postfertilization (dpf), were screened by brightfield microscopy to examine live beating hearts and identify clutches with 25% of progeny exhibiting cardiac arrhythmia. We identified a mutant fitting these criteria and dubbed it *grime* (*uq4ks*) (Fig. 1). Analysis of *grime* mutants versus wild-type siblings with high-speed, brightfield movies showed mutants presented with skipped ventricular beats, irregular beats, and slower heart rate as well as a failure to inflate their swim bladder (Fig. 1 *A–E* and *SI Appendix*, Table S1). While no other gross morphological defects were apparent (Fig. 1*B*), the *grime* mutation was lethal by 15 dpf (*SI Appendix*, Fig. S1). We further investigated whether disturbances in tissue patterning might be causing arrhythmia. We found no differences in the total number of cardiomyocytes and no significant difference was observed in the SAN or AVC cell number in mutants compared with siblings (*SI Appendix*, Fig. S2 *A–C*). Cardiomyocyte membranes were immunostained and area and circularity measured, revealing no significant differences when comparing similar regions of the heart (*SI Appendix*, Fig. S2 *D–F*). Finally, in situ hybridization (ISH) markers for the SAN (*shox2* and *bmp4*), the AVC (*bmp4*), and the outer curvature of the chamber myocardium (*nppa*) were analyzed and found indistinguishable between wild-type and *grime* embryos (*SI Appendix*, Fig. S2*G*). Together these data demonstrate that *grime* mutants have a highly specific arrhythmia phenotype, with hearts otherwise morphologically indistinguishable from wild-type animals.

We next studied phenotypic onset using high-speed imaging. Irregular beats or skipped ventricular beats were observed in ~40% of homozygous mutant embryos as early as 2 dpf and increased to ~80% by 5 dpf (Fig. 1*F*). Interestingly, almost 20% of heterozygous embryos also exhibited these arrhythmias. A tighter correlation between genotype and phenotype was observed when analyzing heart rates: *grime* mutants consistently had 20 to 25%

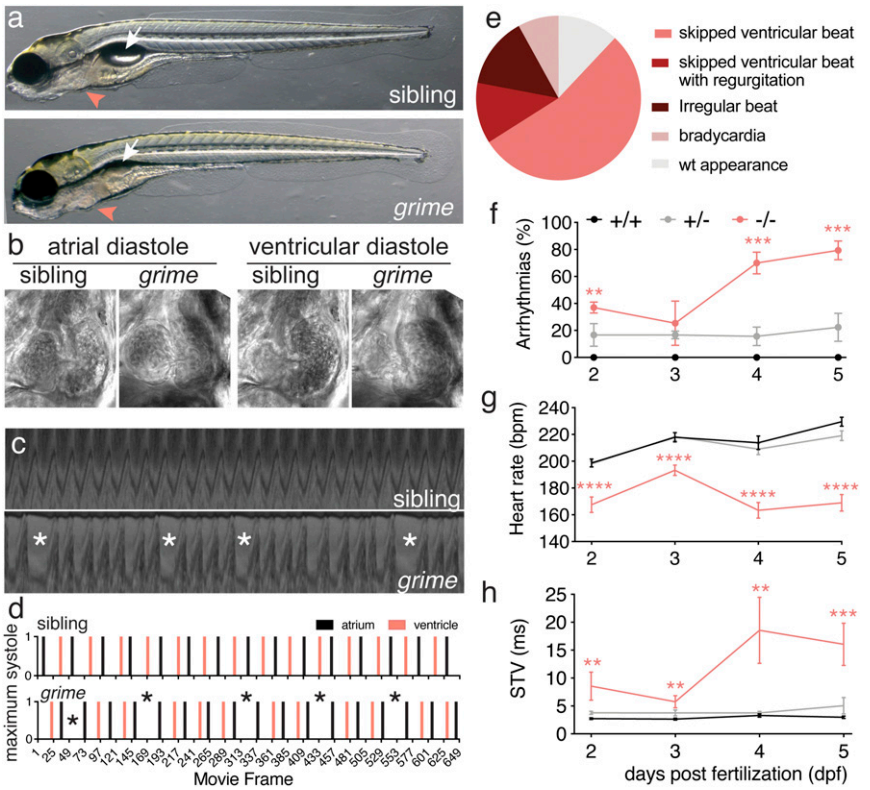

Fig. 1. *grime* mutants display specific cardiac arrhythmia. (*A*) Brightfield lateral view images of wild-type and *grime* (*tmem161b*^{uq4ks}) mutant zebrafish at 5 dpf. The swim bladder of *grime* mutants often fails to inflate (white arrow) but embryos are otherwise indistinguishable (location of the heart depicted by pink arrowhead). (*B*) Frontal view images of live heart by brightfield, high-speed imaging showing sibling and *grime* mutant hearts are anatomically similar both at atrial and ventricular diastole. (*C*) Kymograph of atrial movement versus time from high-speed movies of sibling and *grime* heartbeat. Mutant example shows an embryo with irregular heart rate (single asterisks). (*D*) Graph depicting maximum systole of atrium (black) and ventricle (pink) as a function of time in sibling and *grime* mutants taken from examples Movies S1 and S2. The mutant example shows the skipped ventricular beat phenotype (single asterisks). (*E*) Summary of phenotypes observed in the *grime* mutants at 5 dpf. (*F–H*) Graphs of wild type, heterozygous, and homozygous *grime* mutants at 2 to 5 dpf, showing (*F*) the percentage of embryos presenting with arrhythmias (for more detail, see *SI Appendix*, Table S1) (*G*) heart rates, and (*H*) the STV in atrial contraction interval (mean ± SEM; $n = 20$ to 47; $^{**}P \leq 0.01$, $^{***}P \leq 0.001$, $^{****}P \leq 0.0001$).

lower heart rate compared with siblings at all stages analyzed (1 to 5 dpf; Fig. 1*G* and *SI Appendix*, Fig. S3), including at the onset of peristaltic contraction (*SI Appendix*, Fig. S3*A*). In addition to lower heart rates, *grime* mutants also exhibited increased beat-to-beat interval variation (Fig. 1*H* and *SI Appendix*, Fig. S3*B*). No significant difference was observed for either heart rate or variation between heterozygous and wild-type siblings, despite the observed irregular or skipped beats. These data demonstrate that *grime* is required for correct heart rate and rhythm from the very onset of heart contraction.

Mutations in *tmem161b* Cause the *grime* Arrhythmia Phenotype. To map the genetic lesion responsible for the *grime* phenotype, we undertook whole-genome sequencing mapping and mutation detection (16, 17). Whole-genome sequencing was performed on pooled mutant embryos and bioinformatic analysis was performed to identify regions of homozygosity within the population (i.e., decreased recombination frequency). This established linkage on chromosome 5 and bioinformatic analysis of coding sequences within the linkage region identified a premature stop codon in the transmembrane domain protein, *tmem161b*, predicted to truncate the final 19 amino acids (C466*; Fig. 2 *A*–*C*). To provide stronger genetic evidence, we used CRISPR-Cas9-mediated mutagenesis and generated an additional allele (*uq5ks*), with a premature stop codon in the last transmembrane domain of the *tmem161b* protein. Complementation analysis between *uq5ks* and *grime*/*uq4ks* carriers reproduced the arrhythmia phenotype in compound heterozygotes, confirming the arrhythmia phenotype is caused by mutation of *tmem161b* (Fig. 2 *D* and *E*).

TMEM161B Is Highly Conserved and Required for Normal Cardiac Rhythm in Mice. Tmem161b is predicted to have eight transmembrane domains (18), no other functional domains, and has no ascribed biological function. Tmem161b is a member of a protein family with only two members: Tmem161b and Tmem161a. Tmem161b and Tmem161a are found in all vertebrate species and the common ancestral Tmem161 protein is conserved all the way back to sponge—the very root of the animal kingdom. Interestingly, the Tmem161 proteins are unlike any other proteins, suggesting an invention and fundamental function for this protein family.

Given the remarkable degree of evolutionary conservation in this gene family, we next asked if the role of Tmem161b in cardiac rhythm is conserved in other vertebrates. As no knockout mouse phenotype has been previously reported, we generated a *Tmem161b* knockout mouse. Examination of litters from $Tmem161b^{LacZ/+}$ intercrosses at P7, identified no homozygous $Tmem161b^{LacZ/LacZ}$ mice. At P0, $Tmem161b^{LacZ/LacZ}$ neonates were identified but always found dead (Fig. 3*B*). Dissection of embryos at 17.5 days postcoitum (dpc) identified 25% mutants, suggesting that lethality is occurring perinatally. At 17.5 dpc, embryos were smaller than wild-type and heterozygous littermates and presented with eye defects, in that one of the two eyes remained internal (Fig. 3*A*). Despite the smaller size of homozygous $Tmem161b^{LacZ/LacZ}$ embryos, the hearts of these animals were larger compared with body mass (Fig. 3 *C* and *D*). Measurement of the ventricular chambers from sections showed both increased perimeter and area in $Tmem161b^{LacZ/LacZ}$ embryos (*SI Appendix*, Fig. S4 *A*–*D*) with the interventricular septum significantly wider at the apex (*SI Appendix*, Fig. S4 *A*, *B*, *D*, and *E*). To investigate whether hyperplasia or hypertrophy was responsible for the increased heart size, cardiomyocyte plasma membranes were stained and cell sizes measured. No significant difference in cell size was observed between genotypes in any of the regions analyzed (*SI Appendix*, Fig. S4 *J*–*O*), eliminating hypertrophy as an explanation. We next performed cell counts and observed a significant increase in the number of nuclei in 17.5 dpc $Tmem161b^{LacZ/LacZ}$ hearts, compared with siblings, demonstrating that the increased heart size is caused by hyperplasia (Fig. 3*E*). Finally, to determine whether cardiac fibrosis was responsible for any of the phenotypes we observed in 17.5 dpc $Tmem161b^{LacZ/LacZ}$ hearts, we performed Picrosirius Red staining to detect collagen deposition. While collagen was observed in expected locations (such as valves and vascular

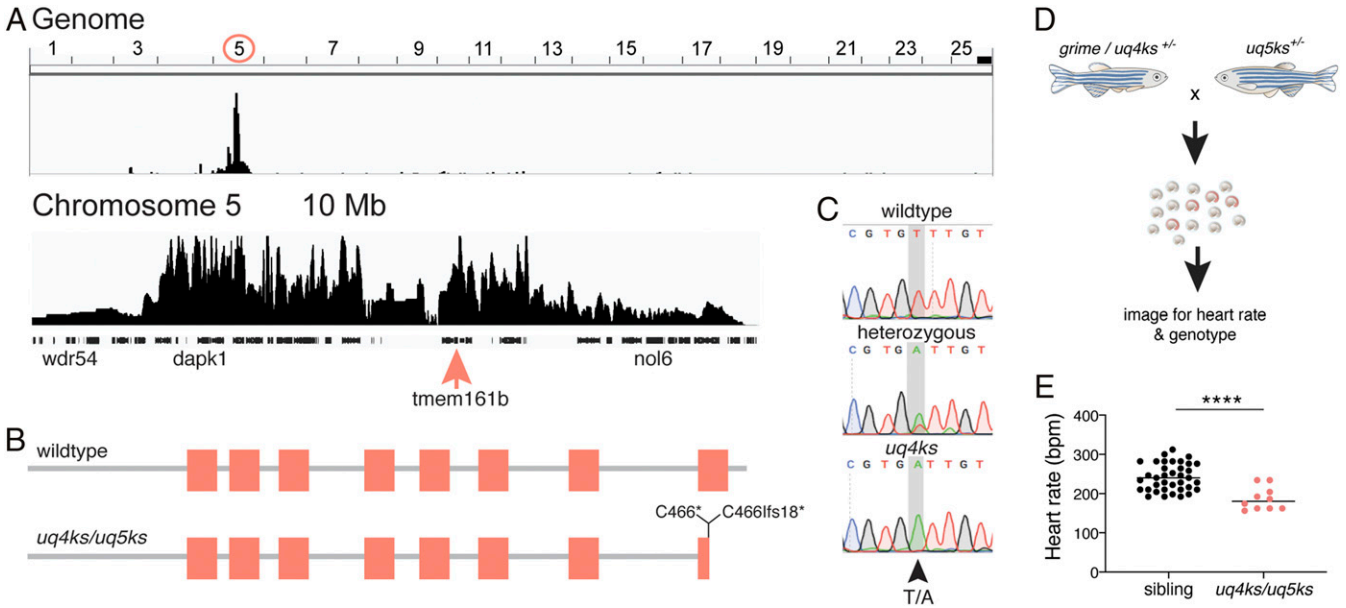

Fig. 2. The arrhythmia phenotype in *grime* is caused by mutation of the *tmem161b* gene. (*A*) Positional cloning of *grime* by whole-genome sequencing mapping shows homozygosity on chromosome 5, and bioinformatic prediction identified a truncating mutation in transmembrane protein 161b, within the linked region (pink arrow). (*B*) Protein schematic of wild-type Tmem161b (above) and mutant alleles (below). The location of the *grime*/*uq4ks* mutation (C466*) and the CRISPR-Cas9-generated *uq5ks* allele (C466Ifs18*) is indicated. (*C*) Sequencing reads from wild-type, heterozygous, and homozygous $tmem161b^{uq4ks}$ animals. (*D*) Experimental setup of complementation assay using a *grime*/*uq4ks* carrier and CRISPR-Cas9-generated *uq5ks* allele. (*E*) Quantification of progeny from complementation assays show that *tmem161b* heterozygosity fails to complement *grime*. Compound heterozygotes (*uq4ks*/*uq5ks*) have a reduced heart rate compared with siblings at 2 dpf, confirming that mutation of *tmem161b* is causative of the cardiac arrhythmia phenotype. $n = 37$ siblings, 10 compound heterozygotes; $^{****}P < 0.0001$.

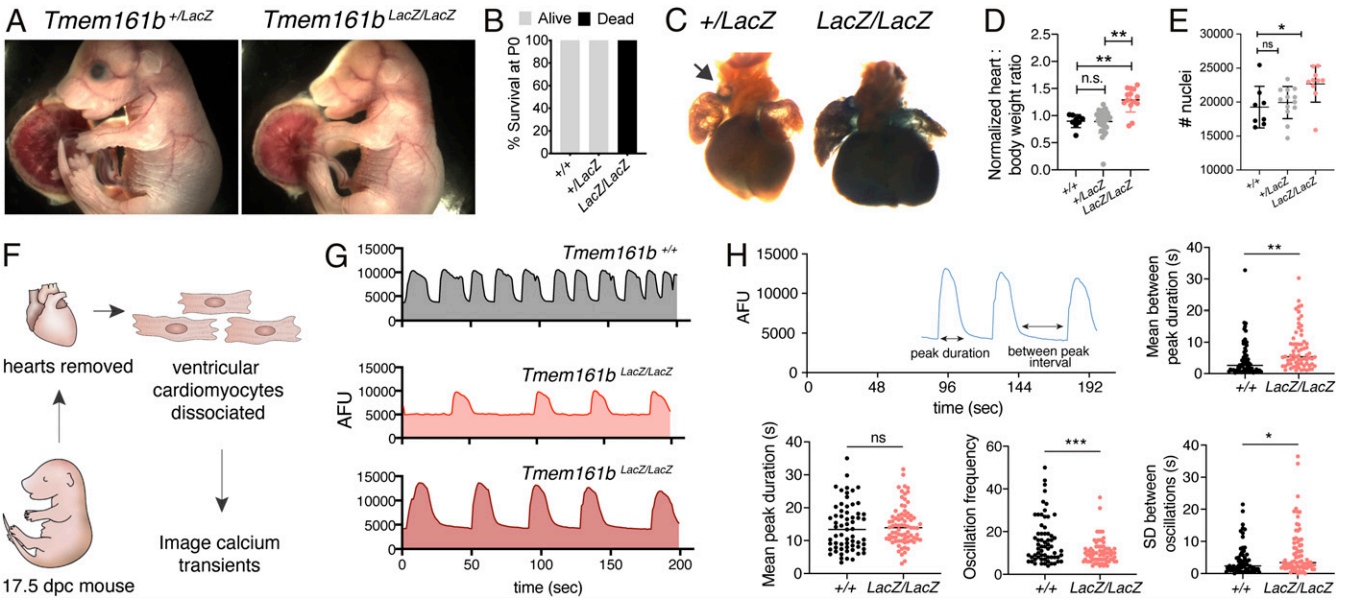

Fig. 3. Tmem161b is required for mouse neonatal survival and wild-type Ca^{2+} oscillations in isolated cardiomyocytes. (*A*) Representative whole embryo images of heterozygous (*Tmem161b*$^{+/LacZ}$) and homozygous (*Tmem161b*$^{LacZ/LacZ}$) *Tmem161b-LacZ* (loss-of-function) mouse embryos at 17.5 dpc. Images show embryonic survival at 17.5 dpc and, with the exception of eye defects, are phenotypically wild type at a gross morphological level. (*B*) Graphical representation of neonatal survival at P0 showing that all *Tmem161b*$^{LacZ/LacZ}$ embryos die at or soon after birth. (*C*) Dissected whole-mount hearts at 15.5 dpc stained for LACZ showing expression throughout the heart as well as in the region of the sinoatrial node (arrow). Homozygous *Tmem161b*$^{LacZ/LacZ}$ hearts appear enlarged compared with heterozygous littermate hearts. (*D*) Graphical representation of heart weight, normalized to body weight, shows an increase in *Tmem161b*$^{LacZ/LacZ}$ hearts compared with *Tmem161b*$^{+/+}$ and *Tmem161b*$^{+/LacZ}$ (at 17.5 dpc). $n = 9$ wild types, 14 homozygotes, and 29 heterozygotes. $^{**}P < 0.001$; $^{*}P < 0.05$. (*E*) Quantification of cardiac cell number shows an increase in *Tmem161b*$^{LacZ/LacZ}$ embryos ($n = 10$) compared with *Tmem161b*$^{+/+}$ ($n = 8$) and *Tmem161b*$^{+/LacZ}$ ($n = 13$) (at 17.5 dpc). $^{*}P < 0.001$. (*F*) Schematic of cardiomyocyte isolation to measure Ca^{2+} transients in mouse embryonic cardiomyocytes. (*G*) Representative traces of Ca^{2+} transients from isolated wild-type and *Tmem161b*$^{LacZ/LacZ}$ cardiomyocytes. (*H*) Overview of parameters measured for cultured single cardiomyocytes stained with the Ca^{2+} indicator Fluo-4 AM and quantification of the rate of Ca^{2+} transients. Increased duration and variation (SD) between oscillations is observed in *Tmem161b*$^{LacZ/LacZ}$ cardiomyocytes compared with wild-type cardiomyocytes. The mean peak duration is unchanged; however the frequency of oscillations (rate) is decreased in *Tmem161b*$^{LacZ/LacZ}$ cardiomyocytes compared with wild type. $n = 63$ to 77 cells from three to four mice. $^{*}P < 0.05$, $^{***}P < 0.01$; n.s., not significant.

smooth muscle) (19) we did not observe any significant collagen deposition in any of the muscular regions of the ventricular wall for any genotypes (*SI Appendix*, Fig. S4 *P–V*). This discounts cardiac fibrosis as a major contributing factor to phenotypes observed at 17.5 dpc. Thus, *Tmem161b* is important in mammals for neonatal survival, for embryonic growth and loss of function causes hyperplastic growth of the embryonic heart.

To investigate whether *Tmem161b* plays a conserved and cell autonomous role in regulating cardiac rhythm, we investigated individual cardiomyocytes ex vivo. Ventricles from 17.5 dpc embryos were dissected and cardiomyocytes dissociated and cultured overnight (Fig. 3*F*). Using the Ca^{2+} indicator Fluo-4 AM, a range of Ca^{2+} dynamics for isolated cells was measured (Fig. 3 *G* and *H*). First, the rate of oscillations for Ca^{2+} cycling was found decreased in mutant cells compared with wild type (Fig. 3 *G* and *H*). Consistently, this coincided with an increase in the time interval between Ca^{2+} transients (Fig. 3 *G* and *H*) and, importantly, the SD in time interval between oscillations was increased in *Tmem161b*$^{LacZ/LacZ}$ cells compared with wild type (Fig. 3 *G* and *H*). This demonstrates that upon disruption of *Tmem161b* in the mouse, cardiomyocytes have decreased beat rate and increased variability in Ca^{2+} cycling; these single-cell resolution phenotypes are consistent with a cardiac arrhythmia phenotype for *Tmem161b* loss-of-function.

Tmem161b Is Specifically Expressed in Excitable Cells at Cardiomyocyte Membranes and Regulates Action Potential Dynamics. To better understand how Tmem161b regulates cardiac rhythm at a mechanistic level, we returned to the zebrafish model. To investigate Tmem161b expression in detail, with subcellular resolution, a transgenic line was generated. The stop codon of *tmem161b* was replaced with a *citrine* cassette, creating a C-terminal fusion protein expressed under the control of the genes endogenous regulatory elements encoded in a bacterial artificial chromosome (BAC) clone (55 kb upstream and 20 kb of flanking sequence downstream). Examination of *Tg(tmem161b*^{BAC}*:tmem161b-citrine)*^{uq24ks} embryos showed strikingly specific expression in tissues that take part in ion exchange, including the heart, ionocytes, and neuromasts (Fig. 4 *A–C*). Closer examination of cardiomyocytes showed Tmem161-Citrine localization at the plasma membrane, colocalizing with cardiomyocyte plasma membrane reporter *Tg(myl7:Cherry-caax)* (Fig. 4*B*). Thus, Tmem161b protein is enriched in excitable cells and at the plasma membrane, a location that is consistent with a role in controlling cardiomyocyte electrical coupling or cycling.

To examine the functional contribution of Tmem161b in cardiomyocyte electrophysiology, we crossed *tmem161b* carriers to the optogenetic voltage indicator line, *Tg(myl7:chimeric VSFP-butterfly CY)*. This line uses voltage-sensitive transmembrane domains situated between the mCitrine and mCerulean fluorescence resonance energy transfer (FRET) pair (5), permitting in vivo analysis of AP shape and propagation across cardiomyocytes (Fig. 5*A*). To visualize AP profiles, FRET signals were graphed relative to time for discrete regions within the heart. Regular cycles of FRET ratio pulses were observed in wild-type animals, commencing from atrium, to AVC, to ventricle for each cycle. For *tmem161b* mutants, skipped ventricular beats appeared as clear atrial and AVC activations, without a ventricular activation at 2 dpf (Fig. 5*B*, asterisk). In these instances, a broader AVC signal was typically observed,

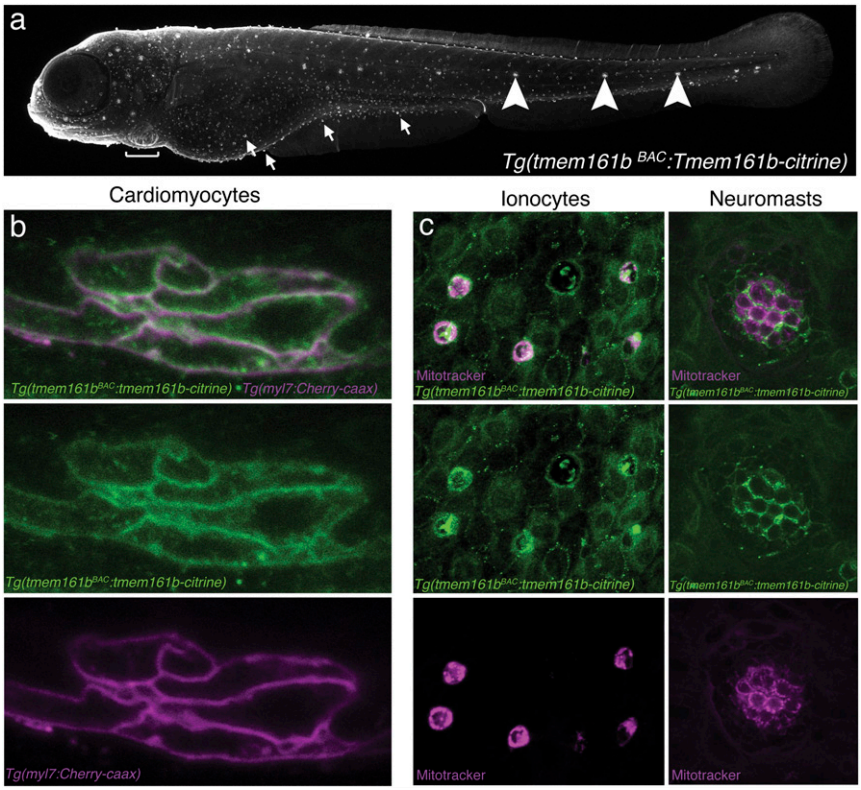

Fig. 4. Tmem161b expression is specific to excitable cells and localizes to plasma membranes. A *tmem161b* BAC transgenic line, *Tg(tmem161b^{BAC}:tmem161b-citrine),* generated by fusing a Citrine cassette to the C terminus of the Tmem161b protein, permits analysis of the *tmem161b* expression pattern as well as protein localization. (*A*) At 5 dpf, *Tg(tmem161b^{BAC}:tmem161b-citrine)* transgenics show Tmem161b-Citrine expression in excitable cells, including cardiomyocytes (bracket), ionocytes (arrows), and neuromasts (arrowheads). (*B*) High-magnification view of ventricular cardiomyocytes at 5 dpf of *Tg(tmem161b^{BAC}:tmem161b-citrine)* embryos crossed to the *Tg(myl7:cherry-caax)* line (cardiomyocyte reporter) shows Tmem161b-Citrine localization at or near the plasma membrane of cardiomyocytes. (*C*) Imaging of ionocytes and neuromasts of *Tg(tmem161b^{BAC}:tmem161b-citrine)* at 5 dpf showing enrichment for Tmem161b-Citrine in these cell types. Ionocyte and neuromast identity are confirmed by staining with Mitotracker (magenta).

sometimes extending into the following AVC depolarization (Fig. 5*B*, arrowhead). SAN irregularities appeared more frequently in 3 dpf analysis and appeared as gaps between consecutive atrial-AVC-ventricular activations (Fig. 5*B*, double asterisks). By overlaying consecutive AP cycles, AP dynamics were measured. At both 2 and 3 dpf, *tmem161b*$^{-/-}$ mutants had increased repolarization time compared with wild-type siblings (Fig. 5*C* and *SI Appendix*, Fig. S4).

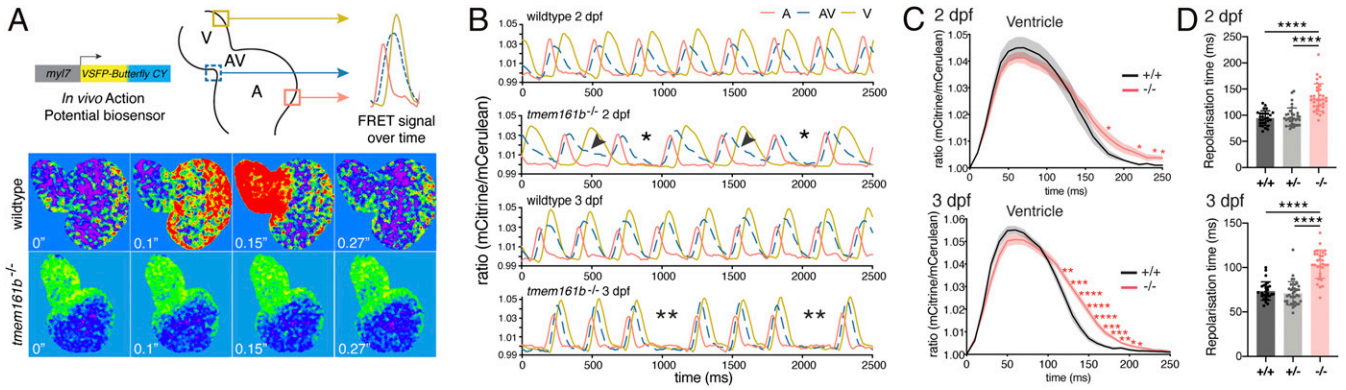

Fig. 5. Tmem161b is required in the zebrafish heart for correct AP repolarization. (*A*, *Top*) Schematic of VSFP-Butterfly biosensor used to report AP dynamics in the live zebrafish heart. (*A*, *Bottom*) Heatmap stills from wild-type hearts showing APs initiating in the atrium and progressing through the ventricle. This is absent in *grime* mutant hearts during arrhythmia episodes. (*B*) AP graphs showing atrial (A), atrioventricular canal (AV), and ventricular (V) activations over time. Examples of 2 dpf wild-type heart and *tmem161b* mutant hearts with skipped ventricular beat and 3 dpf with sinoatrial irregularities are shown. Asterisks indicate missing or delayed activations, black arrowheads indicate prolonged repolarization of an AV-canal AP. (*C*) Average in vivo ventricular AP curves at 2 and 3 dpf for *tmem161b*$^{+/+}$ and *tmem161b*$^{-/-}$ siblings, demonstrating significantly prolonged repolarization in *tmem161b*$^{-/-}$ embryos (mean ± SEM; $n = 8$ to 12). (*D*) Graphs of AP repolarization time for the ventricle at 2 and 3 dpf, showing significantly increased repolarization time. *$P < 0.05$, **$P < 0.01$, ***$P < 0.001$, ****$P < 0.0001$.

AP propagation in the intact heart can be affected by cell-intrinsic mechanisms or cell–cell connectivity. To examine cell-intrinsic behavior at high-resolution, patch-clamp studies were performed. Since *tmem161b*$^{-/-}$ adults are not viable, cardiomyocytes from wild-type and *tmem161b*$^{+/-}$ adult fish were used (Fig. 6*A*). Distinct AP shape changes were observed in *tmem161b*$^{+/-}$ cardiomyocytes compared with wild-type cardiomyocytes (Fig. 6 *B* and *E*). Several measures, such as resting membrane potential, were unchanged by *tmem161b* heterozygosity (*SI Appendix*, Fig. S5), yet a significant shortening of the first repolarization phase (shorter AP duration [APD]$_{20}$) was observed, and yet AP duration at 50 and 90% of repolarization (APD$_{50}$ and APD$_{90}$, respectively) were significantly prolonged (Fig. 6*C*). The increase in APD$_{90}$ was present at pacing frequencies of 2 Hz and lower (Fig. 6*D*). Remarkably, almost all *tmem161b*$^{+/-}$ cardiomyocytes showed early afterdepolarizations (EADs) at 0.2 Hz pacing (Fig. 6*F*). The observed AP phenotype in tmem161b$^{+/-}$ cardiomyocytes with shorter APD$_{20}$ but longer APD$_{50}$ and APD$_{90}$ is relatively uncommon and suggests *tmem161b* is interacting with multiple cardiac ion currents.

To investigate which cardiac ion currents are disturbed in *tmem161b*$^{+/-}$ cardiomyocytes, voltage-clamp experiments were conducted, beginning with the analysis of outwardly directed, repolarizing K$^+$ currents. We focused on the inward rectifier K$^+$ current (I_{K1}) and the rapid delayed rectifier K$^+$ current (I_{Kr}), because the transient outward K$^+$ current (I_{to1}) and slow delayed rectifier K$^+$ current (I_{Ks}) are absent in zebrafish cardiomyocytes (20). I_{K1} was not significantly different between wild-type and *tmem161b*$^{+/-}$ cells. However, we observed a larger outward current at 0 mV and higher test potentials in *tmem161b*$^{+/-}$ cardiomyocytes compared with wild-type cardiomyocytes, indicative of increased I_{Kr} (Fig. 6 *G* and *H*). The increase in I_{Kr} is compatible with the shorter APD$_{20}$ (Fig. 6*C*), which was also found in adult zebrafish hearts in response to the I_{Kr} activator NS1643 (21). The I_{Kr} increase, however, cannot explain the observed prolongation in APD$_{50}$ and APD$_{90}$ and the high incidence of EADs (Fig. 6 *C*, *E*, and *F*). Since changes in Ca^{2+} currents are often associated with EADs, we analyzed the L-type Ca^{2+} current ($I_{Ca,L}$). Indeed, a larger $I_{Ca,L}$ density was measured in *tmem161b*$^{+/-}$ cardiomyocytes compared with wild type (Fig. 6 *G* and *I*).

To identify the specific channels Tmem161b is involved with, we examined the properties of two prominent channels in I_{Kr} and $I_{Ca,L}$, namely HERG/K$_V$11.1 and CACNA1C/Ca$_V$1.2, respectively. K$_V$11.1 and Ca$_V$1.2 were transfected into HEK293T cells, which are otherwise deficient in ion channels. HEK293T cells were transfected with either K$_V$11.1 (*SI Appendix*, Fig. S6) or Ca$_V$1.2 (*SI Appendix*, Fig. S7), with or without TMEM161B. While stereotypical current traces were observed for these channels, there was no effect upon TMEM161B overexpression. We speculate that HEK293T cells lack the necessary interacting partner/s for TMEM161B functionality.

We next examined whether increased channel density at the plasma membrane might be responsible for the increased current

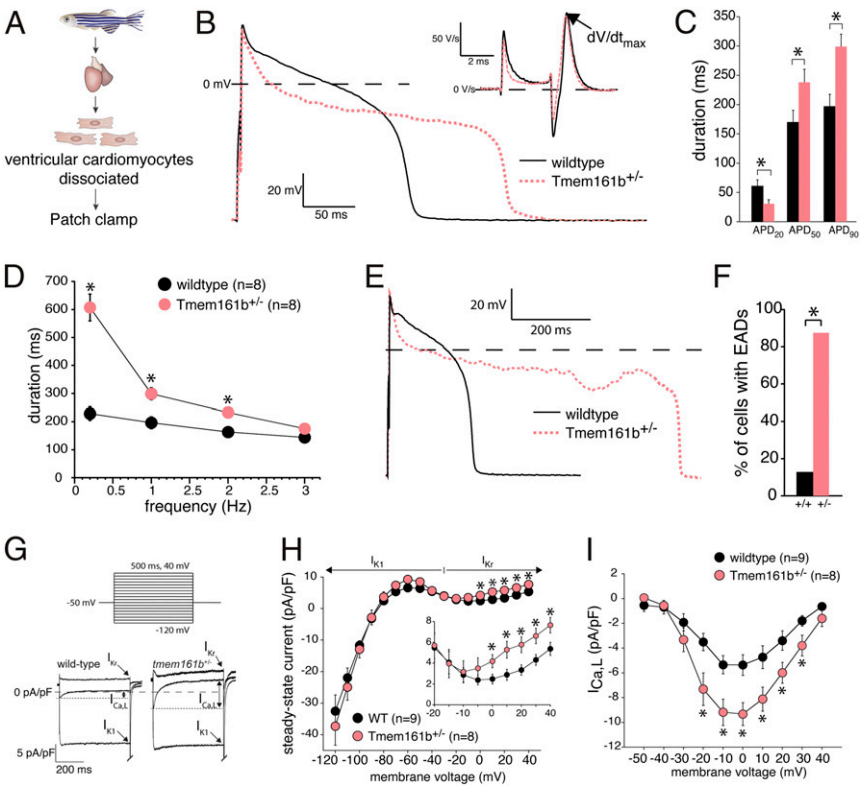

Fig. 6. Tmem161b heterozygosity disrupts wild-type electrophysiology by increasing Ca^{2+} and K^+ current densities in cardiomyocytes. (*A*) Cell isolation approach used for patch-clamp experiments depicted in *B*–*I*. (*B*) Representative APs from patch-clamping of adult cardiomyocytes isolated from adult wild-type and *tmem161b*$^{+/-}$ fish. *Inset* shows first derivative of the AP upstroke and the arrow indicates maximal upstroke velocity (dV/dt$_{max}$). (*C*) Average APDs showing a decrease in APD at 20% repolarization (APD$_{20}$), but an increase in APD at 50 and 90% repolarization (APD$_{50}$ and APD$_{90}$, respectively) in tmem161b$^{+/-}$ cells (pacing at 1 Hz; mean ± SEM, $n = 8$, $^*P < 0.05$). (*D*) Prolonged AP durations are most prominent at low-pacing frequencies. (*E*) Example of APs paced at 0.2 Hz showing EADs in wild-type versus *tmem161b*$^{+/-}$ cells. (*F*) Incidence of EADs is significantly higher in *tmem161b*$^{+/-}$ cells. (*G*, *Top*) Voltage-clamp protocol used to measure the inward rectifier K$^+$ current (I_{K1}), the L-type Ca^{2+} current, and the rapid component of the delayed rectifier K$^+$ current (I_{Kr}). (*Bottom*) Typical net membrane currents at −100 mV (I_{K1}), 0 mV ($I_{Ca,L}$), and +40 mV (I_{Kr}). (*H*) Average current-voltage (I-V) relationships of I_{K1} and I_{Kr} showing no effect on I_{K1}, but an increase in I_{Kr} density in tmem161b$^{+/-}$ cells. (*I*) Average I-V relationships of $I_{Ca,L}$ showing an increase in inwardly directed current in *tmem161b*$^{+/-}$ cells.

density and examined $K_V11.1$ and $Ca_V1.2$ expression by immunofluorescence staining in mouse tissue. Fluorescence intensity of $Ca_V1.2$ or $K_V11.1$ was not significantly different between wild-type, heterozygous, and homozygous *Tmem161b*$^{LacZ/LacZ}$ hearts, either broadly or at the plasma membrane (determined by colocalization with a membrane marker; *SI Appendix*, Fig. S8). These data indicate that changes in $K_V11.1$ or $Ca_V1.2$ expression levels or localization are not responsible for the changes to current densities observed in *tmem161b* loss-of-function cardiomyocytes.

Voltage-gated Ca^{2+} channels have three main gating transitions: closed to open (activation), open to inactivated (inactivation), and inactivated to closed (recovery). Reverse paths are also possible, including inactivated to open (recovery from inactivation). To examine whether the higher $I_{Ca,L}$ densities were a consequence of altered gating properties, we measured voltage dependency of activation and inactivation as well as recovery from inactivation. The increase in $I_{Ca,L}$ density was not accompanied by changes in voltage dependency of activation and inactivation nor by changes in recovery from inactivation (*SI Appendix*, Fig. S9). The role of $I_{Ca,L}$ in setting the zebrafish AP is well known (20, 22, 23). Our observed $I_{Ca,L}$ increase, together with increased I_{Kr}, may contribute to APD_{20} shortening via enhanced Ca^{2+}-dependent $I_{Ca,L}$ inactivation which plays a relevant role under physiological conditions in the zebrafish (23). In addition, the increase in $I_{Ca,L}$, is a logical explanation for the APD_{50} and APD_{90} prolongation as well as the EADs because the inward current during the repolarization phase due to the window current, $I_{Ca,L}$ reactivation, and relief of inactivation, which leads to the so-called U-shaped voltage curve for steady-state inactivation (24), will be increased. Together, these findings indicate that, under healthy conditions, Tmem161b regulates I_{Kr} and $I_{Ca,L}$ in cardiomyocytes and that change in $I_{Ca,L}$ density is not due to altered gating mechanism.

Given that patch-clamp experiments showed that $I_{Ca,L}$ was affected in adult *tmem161b*$^{+/-}$ cardiomyocytes, we returned to the embryo to visualize Ca^{2+} transients in sibling and *tmem161b* homozygous mutants in the live intact heart. For intracellular Ca^{2+} transient measurements, we crossed *tmem161b* carriers to the optogenetic Ca^{2+} sensor, gCaMP6f, under the control of a cardiomyocyte-specific promoter [*Tg(myl7:gal4FF;UAS:GCaMP6f)*] (Fig. 7*A*). Analysis of GCaMP signal intensity over time in 3 dpf embryos allowed examination of Ca^{2+} transient upstroke time (intracellular Ca^{2+} release), Ca^{2+} transient recovery time (reuptake/clearance of Ca^{2+}), as well as maximal Ca^{2+} transient amplitudes (Fig. 7 *B–E*). Upstroke time was significantly faster in the ventricle of *tmem161b* mutant embryos, compared with wild-type siblings (Fig. 7*F*), indicating faster Ca^{2+} release. In line with the patch-clamp data, Ca^{2+} transient amplitude was higher in the atrium and ventricle of *tmem161b* mutant embryos (Fig. 7*G*). Ca^{2+} transient recovery time was prolonged in the ventricle of *tmem161b* mutant embryos compared with their wild-type siblings (Fig. 7*H*). Overall these data indicate that Ca^{2+} release at 3 dpf is faster and increased in *tmem161b*$^{-/-}$ embryos than in wild-type siblings, leading to prolonged recovery times.

Altogether, these studies demonstrate that the *grime* protein, Tmem161b, functions cell autonomously in cardiomyocytes to inhibit both I_{Kr} and $I_{Ca,L}$ currents. This assists in timely action potential repolarization and thereby maintains normal cardiac rhythm from early in embryonic development.

Discussion

In this study, we describe Tmem161b as a regulator of cardiac rhythm and show that it is required for survival in both zebrafish and mice. Tmem161b deficiency in zebrafish causes increased K^+ and Ca^{2+} currents in isolated cardiomyocytes (specifically I_{Kr} and $I_{Ca,L}$, respectively). This has a dramatic effect on the plateau phase of the action potential, prolonging it significantly. EADs are also observed in Tmem161b-deficient cells, consistent with the prolonged plateau phase. In addition to this, Ca^{2+} transients are arrhythmic in both zebrafish and mouse cardiomyocytes and, in zebrafish, increased Ca^{2+} is observed. Together, these data show Tmem161b to be an important regulator of cardiac electrophysiology and vertebrate survival.

In humans, a large proportion of cardiac arrhythmia's are caused by mutations in ion channels or regulators of ion channel function (25). The phenotypes we observe in *tmem161b* mutant zebrafish resemble one such arrhythmia—that of congenital long QT syndrome (LQTS). LQTS is characterized by delayed or prolonged repolarization of the ventricle and symptoms include

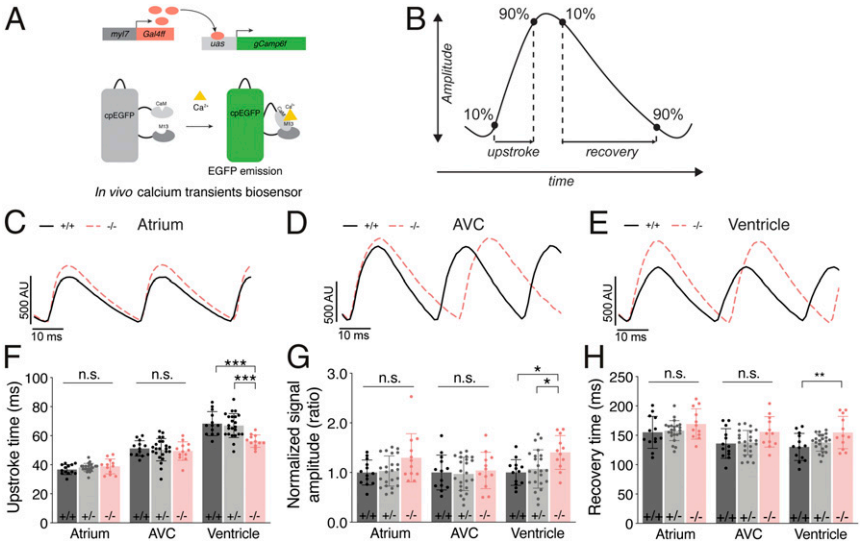

Fig. 7. Ca^{2+} transients are prolonged in *tmem161b* zebrafish mutants. (*A*) Schematic of the GCaMP6f biosensor used to measure in vivo, cardiomyocyte-specific Ca^{2+} transients. (*B*) Ca^{2+} transient parameters. (*C–E*) Representative overlaid Ca^{2+} transients from the (*C*) atrium, (*D*) AVC, and (*E*) ventricle of *tmem161b*$^{+/+}$ and *tmem161b*$^{-/-}$ embryos. (*F–H*) Ca^{2+} transient parameters in 3 dpf *tmem161b*$^{+/+}$, *tmem161b*$^{+/-}$, and *tmem161b*$^{-/-}$ embryos. (*F*) Transient upstroke time, showing a faster upstroke in the ventricle of *tmem161b*$^{-/-}$ embryos. (*G*) Normalized GCaMP6f signal amplitude, demonstrating a higher ventricular Ca^{2+} transient amplitude in *tmem161b*$^{-/-}$. (*H*) Ca^{2+} recovery time, demonstrating a slower reuptake/efflux of Ca^{2+} in *tmem161b*$^{-/-}$ ventricles (mean ± SD; n = 12 to 23; *$P < 0.05$, **$P \leq 0.01$, ***$P \leq 0.001$; n.s., nonsignificant.

syncope, ventricular torsade-de-pointes tachycardia, and sudden cardiac death (26). The ventricular tachycardia occurring in LQTS can be triggered by EADs, which is attributed to increased intracellular Ca^{2+} (27). Given these features, it is tempting to speculate that *TMEM161B* may be a susceptibility locus for LQTS; however, this association remains to be determined. What is clear is Tmem161b is required for survival: Zebrafish larvae die by 15 dpf and mice die at perinatal stages. This is consistent with data from the Genome Aggregation Database (gnomAD) (28), which shows selection against *TMEM161B* loss-of-function variants among human populations. Importantly, homozygous loss-of-function variants are not found in gnomAD for *TMEM161B*, suggesting that homozygous *TMEM161B* loss-of-function is incompatible with human survival.

Mutations in *TMEM161B* have been implicated in human disease, and phenotypes associated with this locus relate mostly to the central nervous system. Genome-wide association studies (GWAS) have identified risk variants near the *TMEM161B* locus for major depressive disorder (29) and attention deficit/hyperactivity disorder (30). Furthermore, heterozygous microdeletions of 5q14, that sometimes include *TMEM161B*, have been reported with syndromic features, including severe mental retardation, seizures, and hypotonia (31). *TMEM161B* has been dismissed as causative of these phenotypes because the minimum common region deleted in these patients does not include *TMEM161B* (32–34). Interestingly, however, several individuals who do harbor deletion of *TMEM161B* also reported with heart defects, including arrhythmia (35–37). Complicating this interpretation is *MEF2C*, which resides in the region adjacent to *TMEM161B* and is an important regulator of heart development (38). Of note, we observed increased incidence of arrhythmia in our heterozygous animals, suggesting that *TMEM161B* may be at least a contributing factor to these individuals' phenotypes.

Tmem161b is predicted to contain eight transmembrane domains but, at present, there are no other annotated protein domains within the protein or regions with homology to annotated domains. The closest homolog to Tmem161b is Tmem161a (this is true for zebrafish, chicken, mice, and human) and it, too, has no annotated domains other than eight predicted transmembrane domains. Interestingly, the common ancestral protein, Tmem161, is found as far back as sponge, suggesting that Tmem161b and Tmem161a represent an ancient and unique protein family. Recent work in *Drosophila* has investigated the common ancestral gene and several consistencies were observed between the homolog and what is reported here for Tmem161b, including altered Ca^{2+} handling upon gene loss of function and increased cell proliferation (39). There are also several differences observed, such as protein localization and altered signaling that is inconsistent with what we observe. We show here that Tmem161b is capable of inhibiting K^+ and Ca^{2+} currents and it does so with specificity: Na^{2+} currents appear unaffected and, furthermore, only I_{Kr} but not I_{K1} are increased upon Tmem161b deficiency. Interestingly, protein localization analysis shows that Tmem161b-Citrine localizes to the plasma membrane of excitable cells, including cardiomyocytes, neuromasts, and ionocytes. This pattern of expression and its effect on action potential is suggestive that it may play a role in modulating action potentials in several excitable tissue types.

In conclusion, we described a regulator of cardiac rhythm. Tmem161b is a transmembrane protein required for wild-type action potentials in cardiomyocytes. Tmem161b deficiency results in prolonged action potential duration and this is caused by increased K^+ and Ca^{2+} currents. Ca^{2+} cycling is also disturbed in the zebrafish heart and this requirement for Tmem161b to regulate Ca^{2+} cycling is conserved between fish and mammals. Interestingly, heterozygous loss of Tmem161b causes arrhythmia in up to 20% of heterozygotes, suggesting this gene may predispose to cardiac arrhythmia phenotypes.

Methods

Animal Lines and Ethical Clearances. Animal work followed guidelines set by the local animal ethics committees at University of Queensland, the Royal Dutch Academy of Sciences, and the University of Melbourne. Zebrafish lines used in this study are Tg(myl7:mCherry-caax) (40), *Tg(myl7:Gal4FF;UAS:GCaMP6f)*, and *Tg(myl7:chimeric VSFP-butterfly CY)* (5), *Tg(myl7:nls-dsred)* (41), and *Tg(fli1a:nuGFP)* (42). The Tmem161b$^{LacZ/+}$ mouse line (Tmem161b$^{tm2a(EUCOMM)Hmgu}$ knockout first reporter tagged allele) was obtained from the Knock-Out Mouse Project (KOMP) Repository (http://www.komp.org/).

Genetic Mapping, CRISPR-Cas9 Mutagenesis, and BAC Transgenesis.
Genetic mapping. Whole-genome sequence-based mapping and mutation detection was performed as previously described (17).
CRISPR-Cas9 mutagenesis. The *uqks5* allele was generated using the guide RNA (gRNA) 5′-GGAGGTGGAGAACAAACACG-3′, with a T7 promoter sequence and a short sequence that overlaps with the constant oligonucleotide as previously described (43). One nanoliter of gRNA (250 ng/μL), nls-zfCas9-nls RNA (500 ng/μL) and phenol red was injected into wild-type one-cell-stage embryos. Injected embryos were grown and founders screened by sequencing.
Genotyping. Genomic DNA of the tmem161b^{uq4ks} and tmem161^{buq5ks} zebrafish was extracted and genotyped using the primers (fwd) 5′-GTGGACACTCGTGGGTGATT-3′ and (rev) 5′-GGCATCCCCTGTTCGTTGAT-3′. For tmem161b^{uq5ks}, PCR reactions were run on 2% sodium borate (SB) gels, discriminating the 13-bp insertion. For tmem161b^{uq4ks} PCR samples were analyzed by Sanger sequencing.
BAC transgenesis. BAC recombineering was performed as previously described (44), integrating a Citrine coding sequence in place of the *tmem161b* stop codon in CHORI BAC clone CH73-286F3. Primer sequences for BAC recombineering were: (fwd) TCTCCACCTCTCTCTTCGGCCTTTTCTACCACCAGTATCTGATGGCTGCAATGGTGAGCAAGGGCGAGGAG and (rev) TTTGAGTGCCTCGTGCTGCAAAGTTCAGTCGAAACAAGCCCTTAAAGATGTCAGAAGAACTCGTCAAGAAGGCG.

High-Speed Brightfield Imaging and Immunostaining. Embryos imaged at 1 dpf were mounted in 1% agarose with no anesthetic. Beyond 1 dpf, 1-phenyl-2-thiourea (PTU)-treated embryos were embedded in 0.3% agarose/E3 medium containing 16 mg/mL tricaine. Recordings were performed at 100 to 150 frames per second (fps) for 10 to 15 s per embryo using a high-speed inverted light microscope or Nikon DE convolution microscope at 28 °C. Heart rate measurements were analyzed using ImageJ. For 2 to 5 dpf quantification in Fig. 1 *D–F*, movies from offspring of three different breeding pairs were analyzed to assess if changes were consistent between pairs and data from all embryos were pooled. Arrhythmias were scored by eye. The short-term variation (STV) of the atrial contraction interval was determined by the following formula: (SUM ΔR-R)/(n*$\sqrt{2}$). In *SI Appendix*, Table S1 heart rates were considered bradycardic when they were 30% lower than the wild-type average heart rate (2 dpf <133 beats per minute [bpm], 3 dpf <145 bpm, 4 dpf <143 bpm, 5 dpf <154 bpm), approximating equivalent parameters in humans (<40 bpm ≡ 30% lower than a resting heart rate of 60 bpm). Hearts were considered to have SAN irregularities when the STV was ≥10% higher than the highest wild-type STV value. AV blocks were identified by eye, by observing the high-speed movies at a low speed.
Immunostaining. Staged embryos were fixed in 4% paraformaldehyde (PFA). Immunofluorescence staining was performed as previously described (40) using chicken anti-GFP (1:200; Abcam) and rabbit anti-dsRed (1:200, Clontech) as primary and anti-chicken Alexa 488 and anti-mouse Alexa 568 (1:200; Invitrogen) as secondary antibodies.
Mitotracker staining. *Tg(tmem161b^{BAC}:tmem161b-citrine)* embryos were incubated in 500 nM of Mitotracker 647/E3 medium in the dark for 30 min at 28 °C. Embryos were washed several times in E3 medium then fixed with 4% PFA and taken through immunofluorescence staining (described above) using an anti-GFP antibody.

Confocal and High-Speed Fluorescence Imaging in Embryos.
Confocal imaging. Immunostained embryos were imaged using the LSM Zeiss 710 confocal microscope with 40× water and 63× oil objectives.
High-speed imaging. *tmem161b^{uq4ks}/tg(myl7:chimeric VSFP-butterfly CY)* and *tmem161b^{uq4ks}/tg(myl7:Gal4FF;UAS:GCaMP6f)* embryos injected with a morpholino (MO) oligomer against *silent heart* (*sih*)/*tnnt2a* (5′-CATGTTTGCTCTGATCTGACACGCA-3′) (45). The 2- to 3-dpf PTU-treated embryos were embedded in 0.3% agarose/E3 medium containing 16 mg/mL tricaine in a heated (28 °C) recording chamber. Recordings were performed using a

custom-build upright widefield microscope (Cairn Research) equipped with a 20× 1.0 NA objective (Olympus XLUMPLFLN). For voltage-sensor fluorescent protein (VSFP) imaging, white LED excitation light was filtered using a 438/24-nm filter (Semrock FF02-438/24-25) and reflected using a 458-nm dichroic mirror (Semrock FF458-Di02-25 × 36). Emitted fluorescence was directed to an emission splitter unit (OptoSplit II ByPass Image Splitter) fitted with a 509-nm dichroic mirror (Semrock FF509-FDi01-25 × 36) and 483/32 nm and 514 long-pass emission filters (Semrock FF01-483/32-25 and LP02-514RU-25, respectively). For GCaMP6f imaging, blue LED excitation light (470 nm) was filtered using a 470/40-nm filter (Chroma ET470/40×) and reflected using a 515-nm dichroic mirror (Chroma T515lp). Emitted fluorescence was filtered by a 514-long pass filter (Semrock LP02-514RU). Images were projected on a high-speed camera (Andor Zyla 4.2 plus sCMOS). Recordings were performed at 100 fps, for 1,000 to 2,000 frames. Recordings were analyzed using ImageJ and Matlab (version R2015a, Mathworks).

Cellular Electrophysiology.

Cell preparation. Single ventricular cells were isolated by an enzymatic dissociation procedure as described previously (46). For this procedure, ventricles from three adult fishes were pooled and stored at room temperature in a modified Tyrode's solution containing (in mmol/L): NaCl 140, KCl 5.4, $CaCl_2$ 1.8, $MgCl_2$ 1.0, glucose 5.5, Hepes 5.0; pH 7.4. Ventricles were cut in small pieces, transferred to Tyrode's solution with 10 μmol/L $CaCl_2$ (30 °C). The solution was refreshed once before the addition of liberase (0.038 mg/mL) and elastase (0.01 mg/mL). During the incubation period, tissue was triturated through a pipette (tip diameter: 2.0 mm). Dissociation was stopped by transferring ventricle pieces into a modified Kraft-Brühe solution (30 °C) containing (in mmol/L): KCl 85, K_2HPO_4 30, $MgSO_4$ 5.0, glucose 5.5, pyruvic acid 5.0, creatine 5.0, taurine 30, β-hydroxybutyric acid 5.0, succinic acid 5.0, bovine serum albumin 1%, Na_2ATP 2.0; pH 6.9 (set with KOH). Tissue pieces were triturated (pipette tip diameter: 0.8 mm) in Kraft-Brühe solution (30 °C) for 4 min to obtain single cells. The cells were stored for at least 45 min in modified Kraft-Brühe solution before placing in a recording chamber on the stage of an inverted microscope (Nikon Diaphot), and superfused with Tyrode's solution (28 °C). Quiescent single cells with smooth surfaces were selected for electrophysiological measurements.

Data acquisition. Voltage control, data acquisition, and analysis were realized with custom-made software. Pipettes (resistance 3 to 4 MΩ) were pulled from borosilicate glass capillaries (Harvard Apparatus) using a custom-made microelectrode puller, and filled with solution containing (in mmol/L): 125 K-gluconate, 20 KCl, 10 NaCl, 0.44 amphotericin-B, 10 Hepes; pH 7.2 (KOH). Potentials were corrected for the calculated liquid junction potential (47). Signals were low-pass filtered with a cutoff of 5 kHz and digitized at 40 and 5 kHz for APs and membrane currents, respectively. Cell membrane capacitance (C_m) was estimated by dividing the time constant of the decay of the capacitive transient in response to 5 mV hyperpolarizing voltage clamp steps from −40 mV by the series resistance.

Membrane currents. The AP measurements, 500-ms depolarizing and hyperpolarizing voltage clamp steps were applied from a holding potential of −50 mV with a cycle length of 2 s. To ensure that the remaining cardiomyocytes in the recording chamber stayed undistorted for biophysical analysis, voltage clamp measurements were performed without specific channel blockers or modified solutions. Inward rectifier K^+ current (I_{K1}) and rapid delayed rectifier K^+ current I_{Kr} were defined as the quasi steady-state current at the end of the voltage-clamp steps at potentials negative or positive to −30 mV, respectively. The L-type Ca^{2+} current ($I_{Ca,L}$) was defined as the difference between peak current and steady-state current at potentials of −50 mV and more positive. Current densities were obtained by normalizing to C_m. Gating properties of $I_{Ca,L}$ were measured with a two-pulse voltage clamp protocol or double-pulse protocol with variable interpulse intervals.

Mouse Embryo Dissection and Histology.

Dissection. Mouse embryos were obtained from timed matings between *Tmem161b*$^{LacZ/+}$ intercrosses, with the presence of a vaginal plug regarded as 0.5 dpc. At 17.5 dpc, embryos were harvested and whole embryo and hearts weighed.

Histology. Hearts were X-Gal stained in whole mount as previously described (48), for visualization of β-galactosidase activity. Samples were then dehydrated and processed for paraffin infusion and embedding. The 7-μm sections were mounted on slides and counterstained with Nuclear Fast Red.

Heart Dissociation and Analysis of Ca^{2+} Transients. For mouse cardiomyocyte dissociation, embryonic hearts were dissected in ice-cold phosphate buffered saline and dissociated into single-cell suspensions using the Neonatal Heart Dissection Kit, mouse and rat (Miltenyi Biotec 130-098-373) and Red Blood Cell Lysis Solution (Miltenyi Biotec 130-094-183), as described previously (49). The cell pellets containing dissociated ventricular cells were resuspended in 300 μL Dulbecco's modified Eagle medium (+10% fetal bovine serum, 1% penicillin-streptomycin, 1× MEM). Cells were plated on coverslips in a 12-well plate and maintained overnight at 37 °C/5% CO_2 for analysis of Ca^{2+} transients.

Fluorescent Ca^{2+} Imaging of Dissociated Cardiomyocytes. Cells were incubated in growth medium containing Fluo-4 AM (10 μM) Ca^{2+} dye for 30 min at 37 °C/5% CO_2 and washed to remove extracellular dye. Single-cell fluorescence (arbitrary fluorescence units [AFUs]) corresponding to changes in intracellular Ca^{2+} concentration were measured using a Nikon Ti-E deconvolution inverted microscope, equipped with a Lumencor Spectra LED lightsource. Images were acquired at 20× objective at 1 Hz (excitation 485 nm, emission 521 nm) for a minimum of 200 s. Only single cardiomyocytes with stable baseline and at least four individual spontaneous Ca^{2+} oscillations (range, 4 to 50) per recording were included in analysis.

Statistical Analyses. Data were analyzed blinded, followed by genotyping where possible. Data are presented as mean ± SEM or SD, as indicated in the figure legends. Statistical analyses were carried out with SigmaStat 3.5 software or GraphPad Prism (v. 8.4.1), using *t* tests for two group analyses and ANOVA for multiple groups. Greater detail about the nature of the analyses for specific assays can be found in *SI Appendix, Supplementary Methods*.

Data Availability. All study data are included in the article and/or supporting information.

ACKNOWLEDGMENTS. This work was supported by research grants from the Australian Research Council and the National Health and Medical Research Council of Australia. Confocal microscopy was performed at the Australian Cancer Research Foundation Dynamic Imaging Centre for Cancer Biology and the Biological Optical Microscopy Platform, with image analysis guidance from Ellie Cho and Shane Cheung. We also acknowledge the support from The Netherlands CardioVascular Research Initiative (CVON): the Dutch Heart Foundation, Dutch Federation of University Medical Centres, The Netherlands Organization for Health Research and Development, and the Royal Netherlands Academy of Sciences (CVON-PREDICT). We thank Y. Onderwater and B. de Jonge for technical assistance and R. Teasdale and J. Vandenberg for helpful discussions. The *Tmem161b*$^{LacZ/+}$ mouse strain used in this research was generated by the trans-NIH Knock-Out Mouse Project (KOMP) and obtained from the KOMP Repository (http://www.komp.org/). NIH grants to Velocigene at Regeneron Pharaceuticals, Inc. (U01HG004085), and the CSD Consortium (U01HG004080) funded the generation of gene-targeted embryonic stem cells for 8,500 genes in the KOMP program and archived and distributed by the KOMP repository at the University of California, Davis. The Alcama antibody (zn-8) was obtained from the Developmental Studies Hybridoma Bank, created by the *Eunice Kennedy Shriver* National Institute of Child Health and Human Development of the NIH and maintained at the University of Iowa.

1. M. S. Rana, V. M. Christoffels, A. F. Moorman, A molecular and genetic outline of cardiac morphogenesis. *Acta Physiol. (Oxf.)* **207**, 588–615 (2013).
2. R. N. Wilkinson, C. Jopling, F. J. van Eeden, Zebrafish as a model of cardiac disease. *Prog. Mol. Biol. Transl. Sci.* **124**, 65–91 (2014).
3. J. G. Wittig, A. Münsterberg, The early stages of heart development: Insights from chicken embryos. *J. Cardiovasc. Dev. Dis.* **3**, 12 (2016).
4. A. P. Kithcart, C. A. MacRae, Zebrafish assay development for cardiovascular disease mechanism and drug discovery. *Prog. Biophys. Mol. Biol.* **138**, 126–131 (2018).
5. C. J. M. van Opbergen *et al*., Optogenetic sensors in the zebrafish heart: A novel in vivo electrophysiological tool to study cardiac arrhythmogenesis. *Theranostics* **8**, 4750–4764 (2018).
6. M. Weber *et al*., Cell-accurate optical mapping across the entire developing heart. *eLife* **6**, e28307 (2017).
7. N. C. Chi *et al*., Genetic and physiologic dissection of the vertebrate cardiac conduction system. *PLoS Biol.* **6**, e109 (2008).
8. M. M. Collins *et al*., Early sarcomere and metabolic defects in a zebrafish *pitx2c* cardiac arrhythmia model. *Proc. Natl. Acad. Sci. U.S.A.* **116**, 24115–24121 (2019).
9. C. A. MacRae, R. T. Peterson, Zebrafish as tools for drug discovery. *Nat. Rev. Drug Discov.* **14**, 721–731 (2015).
10. C. G. Burns *et al*., High-throughput assay for small molecules that modulate zebrafish embryonic heart rate. *Nat. Chem. Biol.* **1**, 263–264 (2005).
11. D. J. Milan, T. A. Peterson, J. N. Ruskin, R. T. Peterson, C. A. MacRae, Drugs that induce repolarization abnormalities cause bradycardia in zebrafish. *Circulation* **107**, 1355–1358 (2003).
12. D. S. Peal *et al*., Novel chemical suppressors of long QT syndrome identified by an in vivo functional screen. *Circulation* **123**, 23–30 (2011).

13. B. J. D. Boukens *et al*., The electrocardiogram of vertebrates: Evolutionary changes from ectothermy to endothermy. *Prog. Biophys. Mol. Biol.* **144**, 16–29 (2019).
14. R. Arnaout *et al*., Zebrafish model for human long QT syndrome. *Proc. Natl. Acad. Sci. U.S.A.* **104**, 11316–11321 (2007).
15. F. Brette *et al*., Characterization of isolated ventricular myocytes from adult zebrafish (Danio rerio). *Biochem. Biophys. Res. Commun.* **374**, 143–146 (2008).
16. J. E. De Angelis *et al*., Tmem2 regulates embryonic Vegf signaling by controlling hyaluronic acid turnover. *Dev. Cell* **40**, 123–136 (2017).
17. K. Koltowska *et al*., mafba is a downstream transcriptional effector of Vegfc signaling essential for embryonic lymphangiogenesis in zebrafish. *Genes Dev.* **29**, 1618–1630 (2015).
18. A. Krogh, B. Larsson, G. von Heijne, E. L. Sonnhammer, Predicting transmembrane protein topology with a hidden Markov model: Application to complete genomes. *J. Mol. Biol.* **305**, 567–580 (2001).
19. D. Wang *et al*., Cardiomyocyte cyclooxygenase-2 influences cardiac rhythm and function. *Proc. Natl. Acad. Sci. U.S.A.* **106**, 7548–7552 (2009).
20. P. Nemtsas, E. Wettwer, T. Christ, G. Weidinger, U. Ravens, Adult zebrafish heart as a model for human heart? An electrophysiological study. *J. Mol. Cell. Cardiol.* **48**, 161–171 (2010).
21. C. M. Hull *et al*., Investigating the utility of adult zebrafish ex vivo whole hearts to pharmacologically screen hERG channel activator compounds. *Am. J. Physiol. Regul. Integr. Comp. Physiol.* **317**, R921–R931 (2019).
22. A. Alday *et al*., Ionic channels underlying the ventricular action potential in zebrafish embryo. *Pharmacol. Res.* **84**, 26–31 (2014).
23. P. C. Zhang, A. Llach, X. Y. Sheng, L. Hove-Madsen, G. F. Tibbits, Calcium handling in zebrafish ventricular myocytes. *Am. J. Physiol. Regul. Integr. Comp. Physiol.* **300**, R56–R66 (2011).
24. J. P. Benitah, J. L. Alvarez, A. M. Gómez, L-type Ca(2+) current in ventricular cardiomyocytes. *J. Mol. Cell. Cardiol.* **48**, 26–36 (2010).
25. J. A. Offerhaus, C. R. Bezzina, A. A. M. Wilde, Epidemiology of inherited arrhythmias. *Nat. Rev. Cardiol.* **17**, 205–215 (2020).
26. Y. Mizusawa, M. Horie, A. A. Wilde, Genetic and clinical advances in congenital long QT syndrome. *Circ. J.* **78**, 2827–2833 (2014).
27. J. R. Skinner, A. Winbo, D. Abrams, J. Vohra, A. A. Wilde, Channelopathies that lead to sudden cardiac death: Clinical and genetic aspects. *Heart Lung Circ.* **28**, 22–30 (2019).
28. K. J. Karczewski *et al*.; Genome Aggregation Database Consortium, The mutational constraint spectrum quantified from variation in 141,456 humans. *Nature* **581**, 434–443 (2020).
29. C. Muench *et al*., The major depressive disorder GWAS-supported variant rs10514299 in TMEM161B-MEF2C predicts putamen activation during reward processing in alcohol dependence. *Transl. Psychiatry* **8**, 131 (2018).
30. C. Liao *et al*., Transcriptome-wide association study of attention deficit hyperactivity disorder identifies associated genes and phenotypes. *Nat. Commun.* **10**, 4450 (2019).
31. B. A. Nowakowska *et al*., Severe mental retardation, seizures, and hypotonia due to deletions of MEF2C. *Am. J. Med. Genet. B. Neuropsychiatr. Genet.* **153B**, 1042–1051 (2010).
32. C. Cardoso *et al*., Periventricular heterotopia, mental retardation, and epilepsy associated with 5q14.3-q15 deletion. *Neurology* **72**, 784–792 (2009).
33. N. Le Meur *et al*., MEF2C haploinsufficiency caused by either microdeletion of the 5q14.3 region or mutation is responsible for severe mental retardation with stereotypic movements, epilepsy and/or cerebral malformations. *J. Med. Genet.* **47**, 22–29 (2010).
34. A. R. Paciorkowski *et al*., MEF2C Haploinsufficiency features consistent hyperkinesis, variable epilepsy, and has a role in dorsal and ventral neuronal developmental pathways. *Neurogenetics* **14**, 99–111 (2013).
35. J. Krishna, T. L. Myers, M. J. Bourgeois, V. Tonk, Interstitial deletion of long arm of chromosome no. 5 with growth hormone deficiency–An emerging syndrome? *Clin. Genet.* **51**, 48–51 (1997).
36. M. C. Silengo, L. Luzzatti, W. R. Centerwall, J. M. Costello, M. Parslow, Interstitial deletion of the long arm of chromosome no. 5 in two unrelated children with congenital anomalies and mental retardation. *Clin. Genet.* **19**, 174–180 (1981).
37. C. Stoll, J. Levy, M. P. Roth, Interstitial deletion of the long arm of chromosome 5 in a deformed boy: 46,XY,del(5)(q13q15). *J. Med. Genet.* **17**, 486–487 (1980).
38. Q. Lin, J. Schwarz, C. Bucana, E. N. Olson, Control of mouse cardiac morphogenesis and myogenesis by transcription factor MEF2C. *Science* **276**, 1404–1407 (1997).
39. X. Ma *et al*., A novel regulator of ER Ca^{2+} drives Hippo-mediated tumorigenesis. *Oncogene* **39**, 1378–1387 (2020).
40. D. R. Grassini *et al*., Myosin Vb is required for correct trafficking of N-cadherin and cardiac chamber ballooning. *Dev. Dyn.* **248**, 284–295 (2019).
41. J. D. Mably, M. A. Mohideen, C. G. Burns, J. N. Chen, M. C. Fishman, Heart of glass regulates the concentric growth of the heart in zebrafish. *Curr. Biol.* **13**, 2138–2147 (2003).
42. B. L. Roman *et al*., Disruption of acvrl1 increases endothelial cell number in zebrafish cranial vessels. *Development* **129**, 3009–3019 (2002).
43. S. J. Capon *et al*., Utilising polymorphisms to achieve allele-specific genome editing in zebrafish. *Biol. Open* **6**, 125–131 (2017).
44. B. M. Hogan *et al*., Ccbe1 is required for embryonic lymphangiogenesis and venous sprouting. *Nat. Genet.* **41**, 396–398 (2009).
45. A. J. Sehnert *et al*., Cardiac troponin T is essential in sarcomere assembly and cardiac contractility. *Nat. Genet.* **31**, 106–110 (2002).
46. F. Tessadori *et al*., Identification and functional characterization of cardiac pacemaker cells in zebrafish. *PLoS One* **7**, e47644 (2012).
47. P. H. Barry, J. W. Lynch, Liquid junction potentials and small cell effects in patch-clamp analysis. *J. Membr. Biol.* **121**, 101–117 (1991).
48. S. Loughna, D. Henderson, Methodologies for staining and visualisation of beta-galactosidase in mouse embryos and tissues. *Methods Mol. Biol.* **411**, 1–11 (2007).
49. A. Ahmed, P. Delgado-Olguin, Isolating embryonic cardiac progenitors and cardiac myocytes by fluorescence-activated cell sorting. *Methods Mol. Biol.* **1752**, 91–100 (2018).